Journal of Applied Physics

RESEARCH ARTICLE | MAY 15 2024

Near-infrared imaging of heat transfer behavior between gadolinium and fluid during magnetization/demagnetization process of magnetocaloric effect

Special Collection: Multicalorics II

The-Anh Nguyen ; Naoto Kakuta ; Ken-ichi Uchida ; Hosei Nagano

J. Appl. Phys. 135, 193904 (2024)
https://doi.org/10.1063/5.0207290
CHORUS

AIP Publishing

Journal of Applied Physics ARTICLE pubs.aip.org/aip/jap

Near-infrared imaging of heat transfer behavior between gadolinium and fluid during magnetization/demagnetization process of magnetocaloric effect

Cite as: J. Appl. Phys. **135**, 193904 (2024); doi: 10.1063/5.0207290
Submitted: 7 March 2024 · Accepted: 2 May 2024 ·
Published Online: 15 May 2024

The-Anh Nguyen,[1] Naoto Kakuta,[2] Ken-ichi Uchida,[3] and Hosei Nagano[1,a]

AFFILIATIONS

[1]Department of Mechanical Systems Engineering, Nagoya University, Nagoya 464-8601, Japan
[2]Department of Mechanical Systems Engineering, Tokyo Metropolitan University, Tokyo 191-0065, Japan
[3]National Institute for Materials Science, Tsukuba 305-0047, Japan

Note: This paper is part of the special topic, Multicalorics II.
[a]**Author to whom correspondence should be addressed:** nagano@mech.nagoya-u.ac.jp

ABSTRACT

This paper reports on the application of a near-infrared (NIR) imaging system for visualizing heat transfer dynamics from a bulk gadolinium (Gd) sample to the surrounding water during the magnetization/demagnetization process of the magnetocaloric effect (MCE). The suggested approach relied on the spectral variation in water absorption band at 1150 nm wavelength within the NIR spectrum. An experimental setup integrated a telecentric uniform-illumination system, a halogen lamp, and an NIR camera to enable real-time monitoring of a single magnetization and demagnetization cycle induced by an external magnetic field, which was generated by a permanent-magnet-based magnetic circuit. Two-dimensional absorbance images captured during this cycle clearly depicted the thermal energy generated by the MCE in water. Furthermore, an analysis of the thermal boundary layer and the quantification of heat transfer from Gd to water provided insights into the dynamics over time. These results indicated the potential of our NIR imaging techniques in optimizing thermal–fluid interactions within MCE systems, thereby improving the design and efficiency of magnetic refrigeration systems.

I. INTRODUCTION

Magnetic refrigeration has developed rapidly during the past three decades as an alternative to vapor compression technology because of its potential from both energy and environmental viewpoints.[1–4] It is a type of solid-state cooling technology that does not use evaporative coolant or mechanical compressors. Specifically, the attained efficiency of this system can reach up to 60% without the need for detrimental fluids.[5] Magnetocaloric effect (MCE) relies on specific magnetocaloric materials that exhibit temperature changes in response to fluctuations in a magnetic field. In recent years, a large number of magnetocaloric materials have emerged as potential candidates for MCE applications, including $(Mn,Fe)_2P$,[6] MnAs,[7,8] polymer-bonded $La(Fe,Si)_{13}$ composites,[9,10] Ni-Mn-based Heusler alloys,[11,12] or $La_{0.8}Sr_{0.2}MnO_3/La_{0.7}Ca_{0.3}MnO_3$ bilayer films,[13] besides the well-established benchmark material, gadolinium (Gd). The MCE is directly related to the magnetic moments within magnetocaloric materials, where the changes in the magnetic field cause these moments to align (entropy decreasing) or disperse (entropy increasing), leading to the generation or absorption of heat [Fig. 1(a)]. One prevalent MCE-based refrigeration technology is the active magnetic refrigeration (AMR), which incorporates the regenerator (such as a parallel plate, a bed of powdered material, or a pin array, all composed of magnetocaloric materials), magnetic field source, heat transfer fluid, and heat exchanger. As illustrated in Fig. 1(b), the AMR system undergoes cyclic magnetization and demagnetization of the magnetocaloric material through the applied

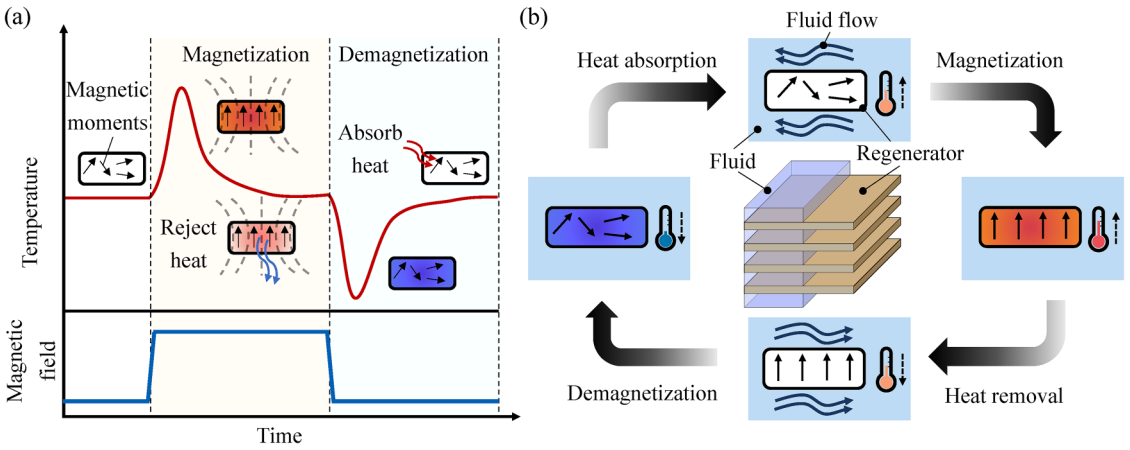

FIG. 1. (a) Magnetocaloric effect (MCE) definition and (b) the schematic of the active magnetic refrigeration (AMR).

magnetic field. During magnetization, the fluid flows from the cold reservoir to the hot, dissipating heat to the surroundings. Subsequently, during demagnetization, as the applied field diminishes, the temperature of the material decreases. At this stage, there is a flow of the fluid from the hot reservoir to the cold, accepting a cooling load. Enhancing how heat moves between the magnetocaloric material and the surrounding fluid, known as thermal–fluid interaction, is crucial for developing better cooling systems. For instance, efficient interaction ensures complete heat removal from the magnetocaloric material during demagnetization, allowing it to absorb more heat in the subsequent magnetization state, resulting in accelerated cooling. Therefore, much research efforts have been directed toward this aspect in recent years to optimize AMR systems for real-world applications.

A growing number of publications focused on numerical models to describe thermal–fluid interaction, mainly in packed-bed and parallel-plate AMR. In the case of the former, Nemec and Levec[14] and du Toit[15] found that the ratio between the outer AMR dimensions and the particle diameter significantly influenced the heat transfer effectiveness. Furthermore, Tusek *et al.*[16] highlighted that the interplay between heat and fluid dynamics primarily depends on the geometry of AMR and the fluid flow rate; this has also been demonstrated in the case of parallel-plate AMR.[17–20] Nielsen *et al.*[18,21] have contributed significantly by developing a technique to estimate the Nusselt scaling factor, offering valuable insights into the relationship between the effective Nusselt number of a specific regenerator and the ideal Nusselt number of a uniformly distributed one. Experimental studies have also been conducted to validate the findings, involving the thermocouple measurement of temperature spans between hot and cold AMRs.[16,22,23] While previous works have made substantial progress in assessing the overall efficiency of AMRs, an experimental research gap exists in comprehensively understanding the interaction between the heat transfer fluid and the magnetocaloric material, which holds the potential for efficiency enhancements. Addressing this limitation necessitates an exploration of transient spatial-resolved data, offering insights into localized heat transfer behaviors and potential areas for improvement. However, only a few studies have delved into this area. Lei *et al.*[24] utilized a Mach–Zehnder interferometer to delineate the dynamics of stagnant fluid behavior within the thermal boundary layer. Although this study provided valuable insights, it is important to acknowledge the challenges associated with the precise alignment of optical components in the Mach–Zehnder interferometer technique, as well as the ability to measure the time-dependent changes in heat transfer rate due to the MCE, both of which remain open areas for further investigation and exploration. To initiate our exploration in this field of research, we employ a promising method known as a near-infrared (NIR) imaging method, which relies on the temperature-dependent absorption band of water in the NIR region. This method operates via transmission and furnishes average temperature assessments along the optical path within water or aqueous solutions. This characteristic makes it suitable for applications where surface measurements are insufficient, allowing the study of the temperature distribution inside the medium and providing more detailed and comprehensive data. Previous studies have confirmed the effectiveness of this method in measuring the temperature of the water and aqueous solutions near various objects without the need for adiabatic conditions, such as thin metal wires,[25] steel spheres,[26,27] micro-magnetic particle layers,[28] and microfluidic channels,[29] achieving a high temperature resolution of better than 0.2 K.

This study aims to establish and validate the NIR imaging system capable of visualizing the heat development from the magnetocaloric material to its surrounding water environment. The experimental setup involved employing a telecentric uniform-illumination system, with the magnetocaloric material being subjected to a magnetization/demagnetization cycle induced by a permanent magnet. The specific magnetocaloric material used in this study was pure Gd slab. Absorbance images at a wavelength of 1150 nm obtained during this cycle were analyzed to derive temperature data, which in turn were utilized for calorimetry

calculations to determine the heat transferred to water. We further discussed the temporal behavior of the thermal boundary layer thickness and heat transfer rate, providing insights for future research directions. The novelty of this study lies in its use of a simple optical imaging configuration, which not only enables real-time monitoring of thermal energy distribution in the heat transfer fluid but also allows for a quantitative assessment of how heat transfer rates evolve over time in the MCE.

Sections II–VI of this paper are organized as follows. In Sec. II, we explain the principles of the NIR temperature imaging technique. Section III describes the experimental methodology, outlining the specific procedures and equipment for data collection. In Sec. IV, visual and quantitative findings from the magnetization and demagnetization processes are presented and analyzed. The discussion on heat transfer is thoroughly explored in Sec. V. Finally, Sec. VI summarizes this study.

II. VARIATIONS IN THE NIR ABSORPTION BAND OF WATER WITH TEMPERATURE

Our previous papers detailed the temperature-related changes in the NIR absorption spectrum of water.[25–27,30] Hence, we provide a concise overview of the theory below. Water molecules exhibit three vibration modes: symmetric stretching (ν_1), symmetric bending (ν_2), and asymmetric stretching (ν_3) of the covalent bonds, each characterized by an absorption peak specific to its distinct frequency [Fig. 2(a)]. The bands detected in the NIR wavelength range (800–2500 nm) solely arise from overtones and combinations of these three modes. These encompass not just basic combinations like $\nu_1 + \nu_2$ but also higher-order combinations such as $\nu_1 + 2\nu_2$.[31] In spectroscopy, the vibration frequency correlates with the absorbed light wavelength. The presence of hydrogen bonds reduces the vibration frequency, shifting the absorption peak toward longer wavelengths in the spectrum. With an increase in temperature, the number of hydrogen bonds decreases, leading to a shift of the absorption band toward shorter wavelengths.

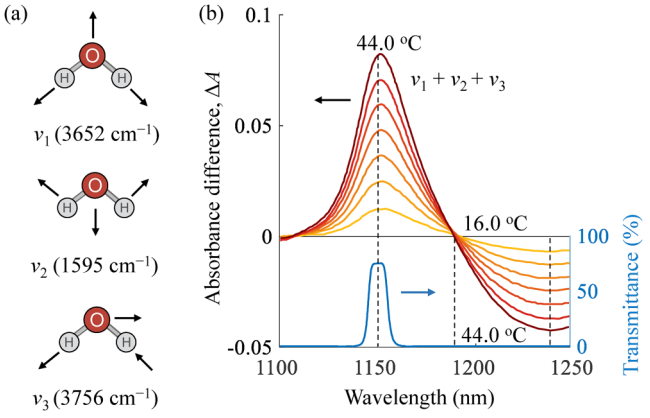

FIG. 2. (a) Three fundamental vibrational modes of water and their wavenumbers. (b) Absorbance difference spectra, $\Delta A(\lambda)$ (left scale) for a 10-mm thick water sample across temperatures ranging from 16.0 to 40.0 °C in 4.0 K intervals (the absorbance at 16.0 °C serves as the reference) and transmittance spectrum (right scale) of the narrow-bandpass filter.[26]

To quantify the amount of light absorbed by a substance at a particular wavelength and temperature, the absorbance, A, and the absorbance difference, ΔA, are used as follows:

$$A(\lambda,\ T) = -\log_{10}\frac{I(\lambda\ ,\ T)}{I_0(\lambda)}, \tag{1}$$

$$\Delta A(\lambda,\ T) = A(\lambda,\ T) - A_r(\lambda,\ T) = -\log_{10}\frac{I(\lambda,\ T)}{I_r(\lambda,\ T)}, \tag{2}$$

where λ is the wavelength of light, T is the temperature of water, and I and I_0 are the intensities of the incident and transmitted light, respectively. I_r is the intensity of transmitted light at a reference state (16.0 °C). Figure 2(b) shows the ΔA spectra (on the left vertical axis) over the temperature range from 16.0 to 44.0 °C with a 2.0 °C increment, where 16.0 °C is A_r. These spectra were around the wavelength range from 1100 to 1250 nm, corresponding to the combination of ν_1, ν_2, and ν_3 ($\nu_1 + \nu_2 + \nu_3$). At approximately 1150, 1193, and 1240 nm (illustrated by dotted lines), there are observable positive peaks, an isosbestic point (ΔA remains constant regardless of temperature), and negative peaks, respectively. We selected the 1150 nm wavelength for temperature imaging in this study due to its highest sensitivity to temperature changes within this wavelength range. The images were detected using a narrow-bandpass filter with a 10 nm bandwidth, with details provided in Sec. III. Furthermore, the spectrum presented in Fig. 2(b) is optimal for water layers with an optical path length ranging from 5 to 20 mm. Specifically, detection becomes saturated when the thickness is below 5 mm and becomes undetectable beyond 20 mm. However, because the various water absorption bands differ in magnitude, they can be selectively employed depending on the thickness. For instance, when the thickness falls between 0.2 and 2 mm, it is preferable to utilize the absorption band resulting from the combination of ν_1 and ν_3 (found within the wavelength range of 1350–1500 nm), as it possesses a higher absorption coefficient compared to the $\nu_1 + \nu_2 + \nu_3$ absorption band.[28]

III. EXPERIMENTAL DETAILS

A. Sample preparation

The measurement sample involved the use of Gd, a commonly utilized material in AMR systems, and a quartz cell with inner dimensions of $30 \times 10 \times 45$ mm^3 (the optical path length is 10 mm), as shown in Fig. 3(a). The advantages of Gd-based alloys lie in their well-defined properties and high MCE near room temperature. A commercial-grade rectangular prism of Gd (Neco-DyUmn, Japan) measuring $5 \times 10 \times 5$ mm^3 was prepared and polished using an automatic polishing machine (MA-150; Musashino Denshi Corp., Tokyo, Japan) [Fig. 3(a)]. This prism was affixed to the central rectangular hole of a plastic holder and securely bonded to the bottom surface of the quartz cuvette. Distilled water was injected into the cuvette using a syringe with a total volume of 6 ml. The cuvette was then covered with a plastic cap. The initial water temperature was set to 20 °C, matching the room

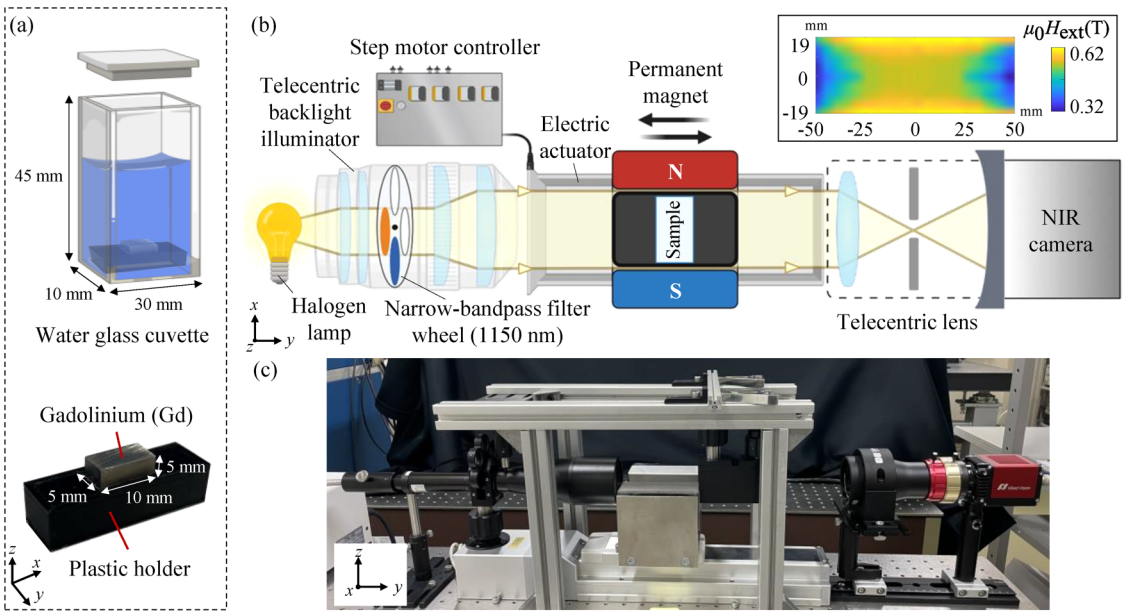

FIG. 3. (a) Dimensions of a water cuvette and a rectangular prism of gadolinium (Gd). (b) Schematic of the experimental apparatus. The inset shows the magnetic flux density. (c) Photograph of the experimental device.

temperature. During the experiment (approximately 200 s), the room temperature was carefully monitored and maintained at 20 °C using a standard air conditioner. The high heat capacity of the water ensured that its average temperature remained close to the initial 20 °C throughout the experiment.

B. Apparatus

Figures 3(b) and 3(c) show a schematic and a photo of the imaging setup. A halogen lamp (FHL-102; Asahi Spectra, Japan) emitted light along the x axis, passing through a telecentric backlight illuminator composed of a 1X collimator lens (RLQL80-1; Asahi Spectra, Japan) and a telecentric lens unit (TOU-1-31; Asahi Spectra, Japan); this system increased the edge contrast of the sample and made the light parallel and homogeneous within a $31 \times 31\ \text{mm}^2$ area. The narrow-bandpass filter (65–785; Edmond Optics) allowed light at $\lambda = 1150$ nm to be incorporated into the filter wheel. The light beam was detected using an InGaAs short-wave infrared camera (Goldeye G-033 TEC1; Allied Vision, Canada). The camera has a pixel pitch of $15 \times 15\ \mu\text{m}^2$ and a 640 (horizontal) × 512 (vertical) pixels. The auto-brightness functionality in the NIR camera settings was adjusted dynamically from frame to frame. To prevent perspective errors, we used a telecentric lens system with a 0.36× magnification (58–257; Edmond Optics), which was positioned between the sample and the camera, maintaining spatial resolution at about 40 μm based on pixel size and magnification.

A U-shaped magnetic circuit was used to generate a magnetic field comprising two Nd–Fe–B permanent magnets (Niroku Seisakusho Co., Ltd., Japan) and a ferromagnetic yoke. The gap between the Nd–Fe–B magnets is 38 mm, and the dimensions of the magnetic poles are $101.6 \times 65.8\ \text{mm}^2$. A Tesla meter (MG-801; Magna, Japan) was utilized to evaluate and visualize the external magnetic flux density distribution, $\mu_0 H_{ext}$ within this air gap, where H_{ext} is the applied external field and μ_0 is the vacuum permeability. The results are mapped in the inset in Fig. 3(b). This magnetic circuit was installed on an electric actuator slider with a step motor to create a linear reciprocation motion. The sample (described in Sec. III A) was hung on a steel frame 15 mm above the optical table.

In consideration of the four states of the MCE, detailed in Sec. I, the experimental process involved four primary stages.

(1) Magnetization: The magnet was accelerated toward the sample utilizing the electric actuator; the initiation of movement marked the time origin, $t = 0$. It took approximately 0.5 s for the sample to reach the center of the two poles, where a magnetic field of up to 0.56 T was generated [as illustrated in the inset of Fig. 3(b)].
(2) Heat rejection: Sustaining the magnetic field for 100 s allowed the sample to attain thermal equilibrium with the surroundings.
(3) Demagnetization: The magnetic field was gradually reduced from 0.56 T to zero by retracting the magnet from the sample at the same speed employed during the magnetization process.
(4) Heat absorption: The magnet was propelled away from the sample and subsequently returned to its original position.

A software (Vimba; Allied Vision, Canada) was utilized to capture a real-time sequence of twelve-bit digital images, comprising multiple frames at a rate of 30 frames per second, saved in the

tiff format. MATLAB R2023a (MathWorks, MA, USA) was used for the subsequent image analysis.

Before the MCE measurement, we confirmed that the magnetic field does not affect the water in this study. This verification is vital due to the Moses effect, wherein the surface of a diamagnetic liquid undergoes distortion when exposed to a magnetic field. Since water is diamagnetic, exposing it to a magnetic field of significant strength can influence the behavior of water molecules, especially in terms of their vibrational states and interactions. This influence can result in observable changes in the NIR spectrum due to modifications in the molecular vibrations or their responses to the magnetic field.[32,33] The procedure and results are shown in Appendix.

IV. TIME-DEPENDENT MAGNETIZATION/ DEMAGNETIZATION IMAGING

A. 2D temperature distribution estimation

The light intensity image detected by the NIR camera after transmitting to the narrow-bandpass filter at $\lambda = 1150$ nm, $I_f(x,\ z)$, is expressed as follows:

$$I_f(x,\ z) = \int_{\lambda_1}^{\lambda_2} \tau(\lambda) I(\lambda; x,\ z)\mathrm{d}\lambda = \int_{\lambda_1}^{\lambda_2} \left[\tau(\lambda) I_0(\lambda; x,\ z) \times 10^{-A(\lambda; x,\ z)}\right]\mathrm{d}\lambda, \tag{3}$$

where $\tau(\lambda)$ is the transmittance spectrum of the narrow-bandpass filter [depicted on the right vertical axis in Fig. 2(b)]. λ_1 and λ_2 denote the minimum and maximum wavelengths of the narrow-bandpass filter, respectively. Then, the absorbance difference image for this filtered measurement is defined in the same manner as Eq. (2),

$$\Delta A_f(x,\ z) = -\log_{10} \frac{I_f(x,\ z)}{I_{f,r}(x,\ z)}, \tag{4}$$

where $I_{f,r}(x,\ z)$ is the reference for $I_f(x,\ z)$, and it was acquired by averaging 50 frames before starting the MCE measurement. Based on the proportional relationship between T and A, along with the

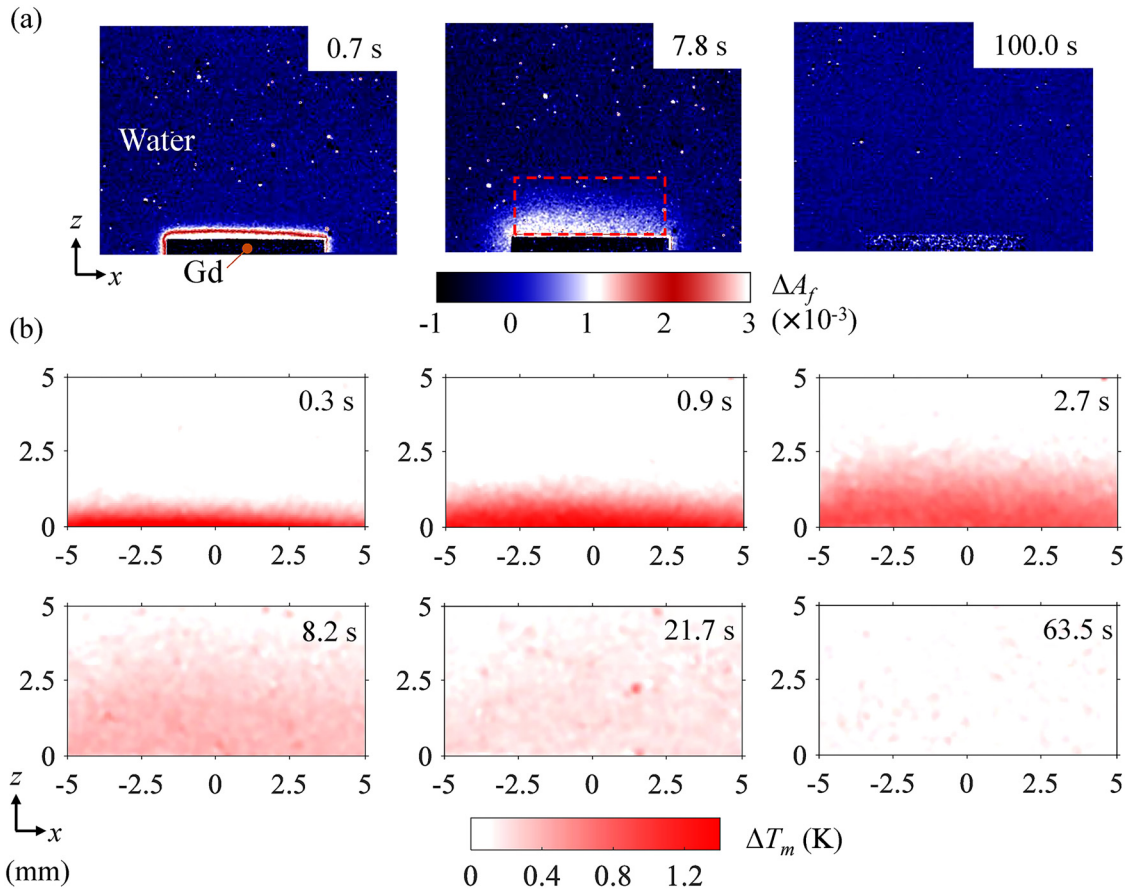

FIG. 4. (a) $\Delta A_f(x,\ z)$ images and (b) enlargement of $\Delta T_m(x,\ z)$ in the red dashed rectangle in (a) during heating mode.

assumption of uniform temperature along the light path (the mean value), the temperature difference, ΔT_m, images can be determined as follows:

$$\Delta T_m(x,\ z) = \frac{\Delta A_f(x,\ z)}{\alpha d}, \tag{5}$$

where d is the optical path length and α is the temperature coefficient, which has a value of $2.76 \times 10^{-4}\ \mathrm{K}^{-1}\ \mathrm{mm}^{-1}$ at 1150 nm.[34] To enhance the quality of the data by mitigating noise or fluctuations, we achieved spatial smoothing through a 3×3 mean filter, while temporal smoothing employed an 11-point fifth-order Savitzky–Golay filter.

B. Results

The magnetization state was examined by observing a sequence of $\Delta A_f(x,\ z)$ images capturing the application of a magnetic field to Gd over a duration of 100 s, as shown in Fig. 4(a). Due to the backlight illumination used in this experimental setup, small debris particles in the water cast shadows with lower intensity values, indicating higher absorbance values compared to their surroundings. These were observed as certain bright dots in the images. Additionally, the presence of black dots was attributed to static artifacts resulting from light scattered by dust particles on the surface of the cuvette. To provide a detailed view of the thermal distribution within the water during the magnetization state, enlarged 2D temperature estimation images, $\Delta T_m(x,\ z)$ were obtained using Eq. (5) [Fig. 4(b)]. As the magnet approached the Gd sample at $t = 0.3$ s, causing alignment of magnetic moments, the temperature of the Gd rose, initiating heat transfer from Gd to the water. This heat transfer continued, gradually increasing the temperature of the water. Following the peak at $t = 0.9$ s, the temperature gradually began to decrease toward ambient conditions due to thermal dissipation. This state demonstrated a steady decrease in temperature, eventually reaching thermal equilibrium around $t = 63.5$ s. No further temperature changes were observed at this point, indicating that the heat exchange rate with the surroundings balanced the heat generation rate within the material.

Figures 5(a) and 5(b) depict $\Delta T_m(z)$ plots at different positions and time points within the water region. In Fig. 5(a), the $\Delta T_m(z)$ profiles at the central axis ($x = 0$ mm) exhibited a notable increase near the vicinity of the Gd surface at $t = 0.3$ s, reaching a maximum at 1.38 K by $t = 0.9$ s, and gradually diminishing to zero by $t = 63.5$ s due to heat loss to the surrounding water. Additionally, the observed decrease in ΔT_m with increasing distance from Gd validated heat diffusion from the source. Abnormal peak values, e.g., $z = 1$ mm, were observed and attributed to the presence of dust particles; these particles dispersed over time due to temperature gradients. It is noteworthy that the observed peak ΔT_m (1.38 K) closely approximated 81% of the expected maximum value of the adiabatic temperature change in pure Gd reported by Almeida *et al.*,[35] within an external magnetic field of 0.6 T. This deviation can be attributed to two factors. First, the orthorhombic prism shape of the Gd sample utilized in our experiment may have influenced the internal magnetic field within the material, resulting in a reduction compared to the externally applied field.[36,37] Second, the dynamics of heat transfer between Gd and the surrounding water, as discussed in Sec. V, contributed to reducing the temperature change experienced by Gd.

In Fig. 5(b), $\Delta T_m(z)$ across five positions along the x axis ($x = -5$, -2.5, 0, 2.5, and 5 mm) at $t = 0.9$ s and $t = 3.3$ s, respectively, were examined. Notably, the peak $\Delta T_m(z)$ values were nearly identical at all five positions, measuring approximately 1.3 K at $t = 0.9$ s and 0.65 K at $t = 3.3$ s. This uniformity suggested consistent

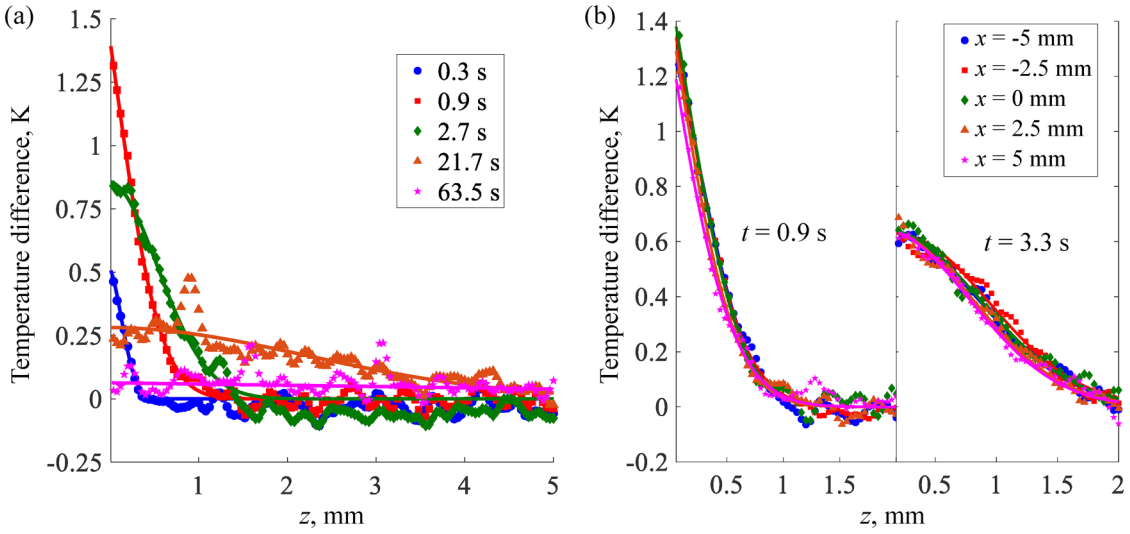

FIG. 5. Vertical line profiles of $\Delta T_m(z)$ and their fitting curves (4th-order polynomial function) in the water region at (a) the central axis ($x = 0$ mm) and (b) five positions along the x axis ($x = -5$, -2.5, 0, 2.5, and 5 mm) at $t = 0.9$ and 3.3 s, respectively.

thermal behavior within the water region, implying a likely uniform temperature distribution across the Gd surface. The slight discrepancy among the plots and curves at $t = 0.9$ and 3.3 s further emphasized the predominance of thermal conduction in the process.

Figure 6 illustrates the demagnetization state, where the gradual reduction of the magnetic field applied to Gd is accompanied by a decrease in its temperature. This observed temperature drop was a direct consequence of the magnetic moments returning to their random orientation. As they relaxed, the previously absorbed energy was released back into the surroundings, primarily in the form of heat transferred to the water. This heat transfer effectively lowered the internal energy of Gd, resulting in its cooling. Similar to the magnetization process, vertical line profiles of $\Delta T_m(z)$ at various positions along the x axis and different time points were utilized to provide quantitative insights into the temporal variations, as shown in Fig. 7. In Fig. 7(a), following the withdrawal of the magnetic field from Gd at $t = 100.3$ s, an immediate decrease in temperature near the Gd surface was observed, $\Delta T_m = -0.79$ K. This was followed by a further drop of 0.48 K over the subsequent 0.6 s, reaching a maximum $\Delta T_m = -1.27$ K. As Gd lost thermal energy to the water, it began to warm up again due to heat exchange with the surroundings. This increasing trend continued until thermal equilibrium was reached around $t = 163.5$ s, where the temperature stabilized. In Fig. 7(b), five vertical $\Delta T_m(z)$ profiles ($x = -5$, -2.5, 0, 2.5, and 5 mm) at $t = 100.9$ s and $t = 103.3$ s exhibited almost identical behavior within each time point. These findings underscored the continued dominance of thermal conduction in the demagnetization state, mirroring the findings from the magnetization state.

Figure 8 shows the comparison plot between the average temperature difference near the vicinity of the Gd surface, $\overline{\Delta T_s}$, and the temperature difference at the center of the Gd surface recorded by a T-type thermocouple, ΔT_c. Based on the discussion in Figs. 5(b) and 7(b), we can derive the values of $\overline{\Delta T_s}$ using an averaging calculation method,

$$\overline{\Delta T_s} = \frac{1}{W}\sum_{i=1}^{W} \max\left(\Delta T_m^i(z)\right), \tag{6}$$

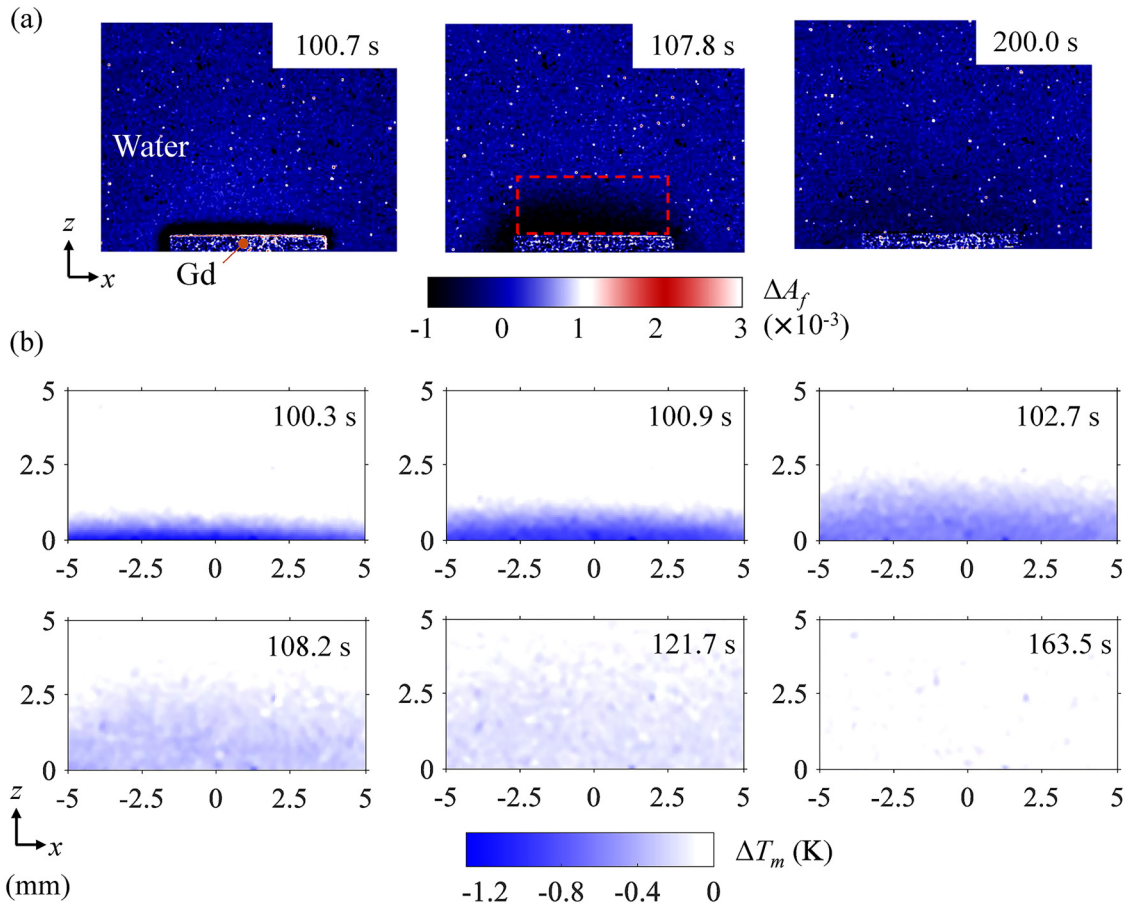

FIG. 6. (a) $\Delta A_f(x, z)$ images and (b) enlargement of $\Delta T_m(x, z)$ in the red dashed rectangle in (a) during cooling mode.

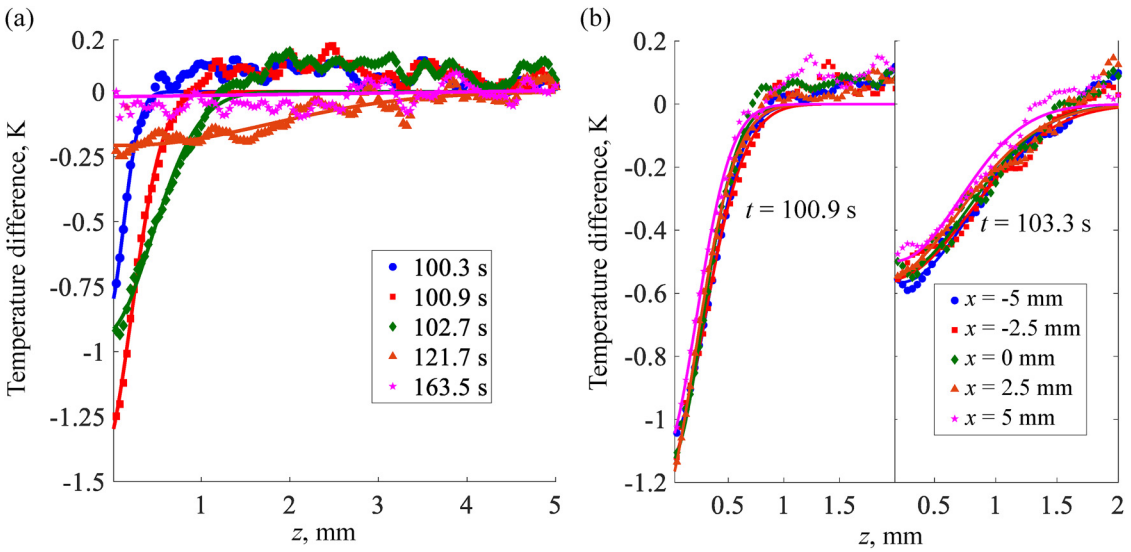

FIG. 7. Vertical line profiles of $\Delta T_m(z)$ and their fitting curves (4th-order polynomial function) in the water region at (a) the central axis ($x = 0$ mm) and (b) five positions along the x axis ($x = -5$, -2.5, 0, 2.5, and 5 mm) at $t = 100.9$ and 103.3 s, respectively.

where W is the $\Delta T_m(x,\ z)$ image width. The comparison demonstrated a close agreement between the two data, indicating the reliability of our methodology. However, we observed discrepancies (up to 78 mK) in the $\overline{\Delta T_s}$ during the magnetic field-on and field-off states. This irreversibility can primarily be attributed to the slow cycling process employed in the experiment, wherein the initial temperature of Gd during demagnetization approached nearly the same level as during magnetization. According to the reversibility of the MCE, the adiabatic temperature changes during magnetization, $\Delta T_{ad,mag}$, and demagnetization states, $\Delta T_{ad,demag}$, follow the relation: $\Delta T_{ad,mag}(T) = -\Delta T_{ad,demag}(T + \Delta T_{ad,mag}(T))$.[38] Consequently, at the same initial temperature (20 °C), $\Delta T_{ad,mag}$ could be slightly higher than $\Delta T_{ad,demag}$, consistent with this study.

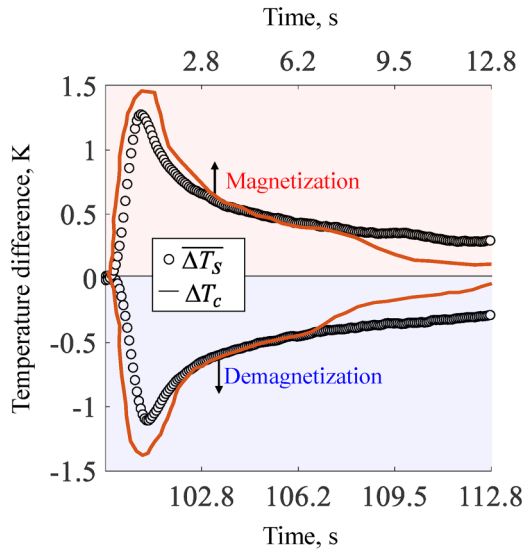

FIG. 8. Comparison of $\overline{\Delta T_s}$ and ΔT_c.

V. THERMAL ENERGY TRANSFER ANALYSIS

The spatial-temporal temperature distribution images obtained during the magnetization and demagnetization states provide valuable insights into the heat transfer dynamics within the system. In this section, we will focus on the thermal boundary layer development and the thermal energy transferred into the heat transfer fluid, i.e., water, in the region of interest within the red dashed rectangle (10×5 mm^2) in Figs. 4(a) and 6(a).

Figure 9 shows the definition of thermal boundary layer thickness based on the analysis of binary images. Thermal boundary layer refers to the region near a surface where the temperature gradient transitions from the boundary condition (e.g., the surface

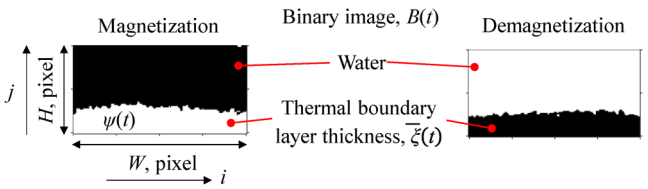

FIG. 9. The definition of thermal boundary layer thickness using the binary image.

temperature) to the surrounding temperature. In this study, the Otsu method was employed for thresholding, enabling the identification of an optimal threshold that minimizes the intraclass variance of thresholded black and white pixels.[39] Subsequent to thresholding, individual images at discrete time intervals were transformed into binary ones, $B(t)$, with values of one and zero denoting white and black regions, respectively. Then, the calculation of the average thermal boundary layer thickness, $\bar{\xi}$, involved determining the ratio between the area of this layer, ψ, defined by the total count of white pixels during magnetization and, conversely, black pixels during demagnetization, and the image width, W.

Temporal development of $\bar{\xi}$ during magnetization and demagnetization is plotted in Fig. 10(a). We observed that the evolution of $\bar{\xi}$ occurred in two distinct periods. Initially, $\bar{\xi}$ increased gradually throughout 13 s in both cases, with the maximum value of $\bar{\xi}$ was 2.9 and 2 mm for magnetization and demagnetization, respectively. The rate of increase in $\bar{\xi}$ depended on the thermal diffusivity of the fluid and time, consistent with previous studies on purely diffusive cases with flat-surface boundaries.[30,40,41] Indeed, the inset of Fig. 10(a) demonstrates that $\bar{\xi}$ is proportional to $(\kappa t)^{1/2}$, where κ represents the thermal diffusivity of water. As time progressed, heat continued to transfer between Gd and water, leading to a decrease in $\bar{\xi}$. Eventually, the system achieved thermal equilibrium, with the temperature gradient between the Gd surface and surrounding fluid becoming negligible. At this point, the boundary layer essentially vanished, resulting in a uniform temperature distribution

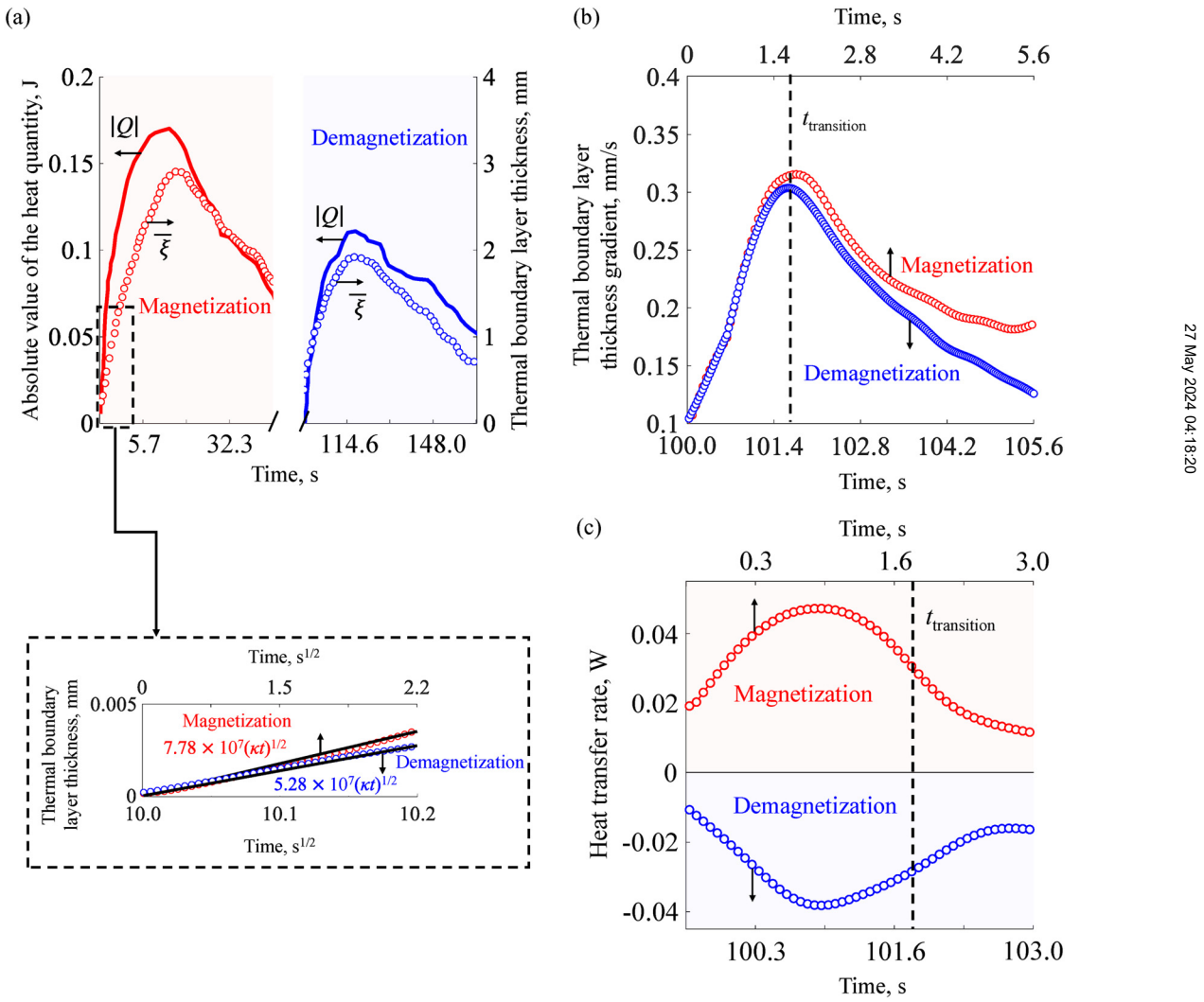

FIG. 10. (a) Dependences of $|Q|$ (left scale) and $\bar{\xi}$ (right scale) on time. The enlargement of $\bar{\xi}$ in the black dashed rectangle with the linear fitting curves. Gradient of (b) $\bar{\xi}$ and (c) Q over time.

across the fluid. This transition in $\bar{\xi}$ correlated with the total amount of heat transferred from Gd to water, Q [the left y axis in Fig. 10(a)]; for clarity, the absolute values of Q were used to ensure that both datasets appear positive. This cumulative heat transfer reflects the amount of energy exchanged between Gd and water. Mathematically, we can express Q as the area-weighted average equation,

$$Q = \iint\int_0^d \rho c \Delta T \, dx dy dz = \rho c \iint \frac{\Delta A_f}{\alpha} dx dz = \frac{\rho c \sigma}{\alpha} \sum_{i,j}^{N} \Delta A_f^{ij} = \frac{\rho c \chi}{\alpha N} \sum_{i,j}^{N} \Delta A_f^{ij}, \quad (7)$$

where ρ is the density and c is the specific heat at constant pressure, both assumed constant: $\rho = 9.93 \times 10^{-7}$ kg/mm^3 and $c = 4180$ J/(kg K). σ is the real area corresponding to one pixel, χ is the real area of the region of interest, N is the number of pixels, and i and j is the image pixel number in the x and z directions, respectively. Because of the irreversibility of this system, as explained in Sec. IV B, Q was not the same in two cases; Q in demagnetization was smaller by approximately 25% compared to the magnetization.

However, it should be noted that a thicker thermal boundary layer or a larger amount of energy transferred to the water corresponded to a reduction in the temperature gradient, as illustrated in Figs. 5(a) and 7(a). This phenomenon implied that heat was transferred over a greater distance, resulting in a slower rate of temperature change across that distance and, consequently, a lower temperature gradient or heat transfer rate. Figure 10(b) shows the behavior of the rate of change in $\bar{\xi}$ over time, represented by the gradient, $\partial\bar{\xi}/\partial t$. It was observed that $\partial\bar{\xi}/\partial t$ increased rapidly for about 1.8 s after both magnetization and demagnetization, suggesting a rapid change in the thermal boundary layer and potentially efficient heat transfer. As time progresses beyond this initial period, the value of $\partial\bar{\xi}/\partial t$ gradually diminished. This decline marked the point at which the heat began to spread more evenly throughout the layer rather than just transferring from the surface to the fluid. The significant transition can be referred to as the onset of heat diffusion, $t_{\text{transition}}$, occurred at 1.8 s for magnetization and 101.8 s for demagnetization. Figure 10(c) shows the heat transfer rate, $\partial Q/\partial t$. As expected, the maximum values of $\partial Q/\partial t$ were observed before $t_{\text{transition}}$, measuring 0.047 and −0.038 W during magnetization and demagnetization, respectively.

Understanding the relationship between the thermal boundary layer thickness and heat transfer efficiency is crucial for optimizing MCE systems, particularly in microchannel parallel-plate regenerators. While initially, a thicker boundary layer might increase the local heat transfer rate due to the larger contact area between the solid surface and the fluid, it can also lead to a decrease in the overall heat transfer rate over time due to factors like increased heat travel distance and potentially reduced temperature gradient. This trade-off needs careful consideration during design. Additionally, addressing flow maldistribution in these microchannels is essential for maintaining optimal cooling or heating performance and upholding the coefficient of performance of the MCE system, as uneven flow can create localized inefficiencies in heat transfer regardless of the thermal boundary layer.[42,43] This aspect will be considered in future research.

VI. CONCLUDING REMARKS

In conclusion, we demonstrated the effectiveness of the NIR imaging method for visualizing and quantifying heat transfer dynamics during an MCE from the magnetocaloric material to the surrounding water. By exploiting the water absorption coefficient variation at 1150 nm, the NIR system effectively captured two-dimensional absorbance images throughout a single magnetization and demagnetization cycle induced by a center magnetic field of 0.56 T, which was generated by a permanent-magnet-based magnetic circuit. Temperature images revealed peak temperature differences of 1.38 and −1.27 K near the Gd surface during magnetization (0.9 s) and demagnetization (100.9 s), respectively. Utilizing binary processing, we determined the thermal boundary layer thickness, observing its increase proportional to the square root of the product of thermal diffusivity of water and time. Additionally, the heat quantity transferred from Gd to water correlated with the development of the thermal boundary layer thickness. Notably, the maximum heat transfer rate of 0.047 and −0.038 W occurred before the onset of heat diffusion at 0.9 and 100.9 s in the magnetization and demagnetization states, respectively. Future research should build upon these findings to explore the broader applicability of NIR imaging to diverse MCE system configurations and operating conditions. This could involve investigating different regenerator geometries, flow rates, and magnetic field strengths to evaluate the thermal–fluid interaction across various scenarios. Exploring various NIR wavelengths may offer insights into alternative heat transfer fluids, such as ethylene glycol, and facilitate the construction of a data set on heat transfer coefficients for assessing the performance of MCE systems. Furthermore, this method shows potential for application beyond MCE, extending to other caloric effects like electrocaloric, elastocaloric, and barocaloric effects, by replacing magnetic fields with electric fields, strain, and pressure.

ACKNOWLEDGMENTS

The authors thank H. Sepehri-Amin, F. Ando, and A. Alasli for valuable discussions. This work was supported by ERATO "Magnetic Thermal Management Materials" (No. JPMJER2201) from JST, Japan.

AUTHOR DECLARATIONS

Conflict of Interest

The authors have no conflicts to disclose.

Author Contributions

The-Anh Nguyen: Conceptualization (equal); Formal analysis (equal); Investigation (equal); Methodology (equal); Writing – original draft (equal); Writing – review & editing (equal). **Naoto Kakuta:** Methodology (equal); Writing – review & editing (equal). **Ken-ichi Uchida:** Funding acquisition (equal); Project administration (equal); Validation (equal); Writing – review & editing

(equal). **Hosei Nagano:** Conceptualization (equal); Funding acquisition (equal); Project administration (equal); Supervision (equal); Validation (equal); Writing – review & editing (equal).

APPENDIX: EFFECT OF MAGNETIC FIELDS ON THE ABSORPTION SPECTRUM OF WATER

A quartz cuvette with inner dimensions of $30 \times 10 \times 45\ \text{mm}^3$ (with an optical path length of 10 mm) was utilized to verify whether the magnetic field affects water itself. Distilled water (6 ml) was injected into the cuvette using a syringe, and the cuvette was sealed with a plastic cap.

Initially, the intensity of transmitted light through the cuvette containing water was measured as a reference state without the magnet and denoted as I_w. Subsequently, this cuvette was placed at the center of the two poles, exposing it to a magnetic field of up to 0.56 T for a duration of 100 s. The intensity of light under this condition was recorded as I_m. The change in absorbance, ΔA, was then calculated using the logarithmic ratio of I_m to I_w: $-\log_{10}(I_m/I_w)$.

Figure 11 shows the plotted ΔA profiles within the white dashed rectangle under the magnetic flux value of 0.56 T. Throughout the entire duration, the resulting absorption data consistently exhibited minimal variation or remained unchanged. Occasional minor deviations in ΔA data were observed, likely attributed to minor impurities in the water or the cuvette. This observation implies that under those experimental conditions (e.g., $\mu_0 H_{\text{ext}} = 0.56$ T and $\lambda = 1150$ nm), any influences of the magnetic field, beyond temperature effects, on ΔA were notably insignificant. This outcome remained consistent when applying another temperature-sensitive wavelength, $\lambda = 1240$ nm, within the 1100–1250 nm range.

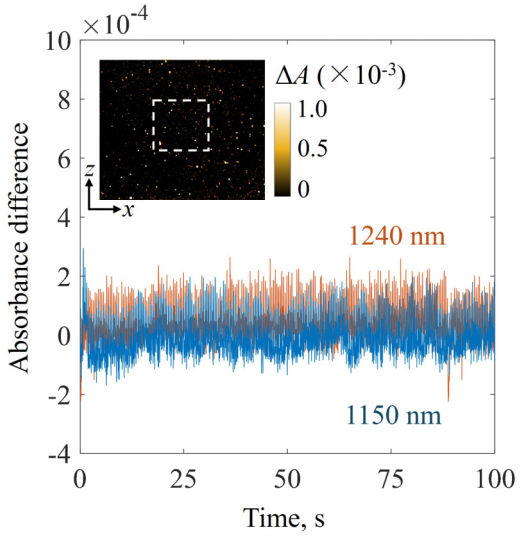

FIG. 11. Temporal changes in the absorbance difference ΔA of water at $\lambda = 1150$ and 1240 nm under 0.56 T for the white dashed rectangular area.

DATA AVAILABILITY

The data that support the findings of this study are available from the corresponding author upon reasonable request.

REFERENCES

[1]H. Johra, K. Filonenko, P. Heiselberg, C. Veje, S. Dall'Olio, K. Engelbrecht, and C. Bahl, "Integration of a magnetocaloric heat pump in an energy flexible residential building," Renew. Energy **136**, 115–126 (2019).
[2]A. Kitanovski, "Energy applications of magnetocaloric materials," Adv. Energy Mater. **10**(10), 1903741 (2020).
[3]X. Moya and N. D. Mathur, "Caloric materials for cooling and heating," Science **370**(6518), 797–803 (2020).
[4]J. Y. Law, L. M. Moreno-Ramírez, Á Díaz-García, and V. Franco, "Current perspective in magnetocaloric materials research," J. Appl. Phys. **133**(4), 040903 (2023).
[5]L. M. Maier, P. Corhan, A. Barcza, H. A. Vieyra, C. Vogel, J. D. Koenig, O. Schäfer-Welsen, J. Wöllenstein, and K. Bartholomé, "Active magnetocaloric heat pipes provide enhanced specific power of caloric refrigeration," Commun. Phys. **3**(1), 1–6 (2020).
[6]O. Tegus, E. Brück, K. H. J. Buschow, and F. R. de Boer, "Transition-metal-based magnetic refrigerants for room-temperature applications," Nature **415**(6868), 150–152 (2002).
[7]H. Wada and Y. Tanabe, "Giant magnetocaloric effect of $MnAs_{1-x}Sb_x$," Appl. Phys. Lett. **79**(20), 3302–3304 (2001).
[8]L. Tocado, E. Palacios, and R. Burriel, "Entropy determinations and magnetocaloric parameters in systems with first-order transitions: Study of MnAs," J. Appl. Phys. **105**(9), 093918 (2009).
[9]H. Zhang, Y. Sun, E. Niu, F. Hu, J. Sun, and B. Shen, "Enhanced mechanical properties and large magnetocaloric effects in bonded La(Fe, Si)13-based magnetic refrigeration materials," Appl. Phys. Lett. **104**(6), 062407 (2014).
[10]K. P. Skokov, D. Y. Karpenkov, M. D. Kuz'Min, I. A. Radulov, T. Gottschall, B. Kaeswurm, M. Fries, and O. Gutfleisch, "Heat exchangers made of polymer-bonded La(Fe,Si)13," J. Appl. Phys. **115**(17), 4–6 (2014).
[11]J. Liu, T. Gottschall, K. P. Skokov, J. D. Moore, and O. Gutfleisch, "Giant magnetocaloric effect driven by structural transitions," Nat. Mater. **11**(7), 620–626 (2012).
[12]R. Modak, R. Iguchi, H. Sepehri-Amin, A. Miura, and K. Uchida, "Simultaneous direct measurements of conventional and inverse magnetocaloric effects in Ni-Mn-based Heusler alloys using lock-in thermography technique," AIP Adv. **10**(6), 065005 (2020).
[13]R. Yuan, P. Lu, H. Han, D. Xue, A. Chen, Q. Jia, and T. Lookman, "Enhanced magnetocaloric performance in manganite bilayers," J. Appl. Phys. **127**(15), 154102 (2020).
[14]D. Nemec and J. Levec, "Flow through packed bed reactors: 1. Single-phase flow," Chem. Eng. Sci. **60**(24), 6947–6957 (2005).
[15]C. G. du Toit, "Radial variation in porosity in annular packed beds," Nucl. Eng. Des. **238**(11), 3073–3079 (2008).
[16]J. Tušek, A. Kitanovski, and A. Poredoš, "Geometrical optimization of packed-bed and parallel-plate active magnetic regenerators," Int. J. Refrig. **36**(5), 1456–1464 (2013).
[17]K. K. Nielsen, J. Tusek, K. Engelbrecht, S. Schopfer, A. Kitanovski, C. R. H. Bahl, A. Smith, N. Pryds, and A. Poredos, "Review on numerical modeling of active magnetic regenerators for room temperature applications," Int. J. Refrig. **34**(3), 603–616 (2011).
[18]K. K. Nielsen, K. Engelbrecht, D. V. Christensen, J. B. Jensen, A. Smith, and C. R. H. Bahl, "Degradation of the performance of microchannel heat exchangers due to flow maldistribution," Appl. Therm. Eng. **40**, 236–247 (2012).
[19]T. Lei, K. Engelbrecht, K. K. Nielsen, and C. T. Veje, "Study of geometries of active magnetic regenerators for room temperature magnetocaloric refrigeration," Appl. Therm. Eng. **111**, 1232–1243 (2017).

[20]Q. Hou, Y. Xuan, W. Lian, Y. Xu, and Y. Ma, "A novel approach for suppressing flow maldistribution in mini-channel heat exchangers," Int. J. Therm. Sci. **184**, 108020 (2023).
[21]K. K. Nielsen, K. Engelbrecht, and C. R. H. Bahl, "The influence of flow maldistribution on the performance of inhomogeneous parallel plate heat exchangers," Int. J. Heat Mass Transfer **60**(1), 432–439 (2013).
[22]J. Tušek, A. Kitanovski, S. Zupan, I. Prebil, and A. Poredoš, "A comprehensive experimental analysis of gadolinium active magnetic regenerators," Appl. Therm. Eng. **53**(1), 57–66 (2013).
[23]T. Xiong, G. Liu, S. Huang, G. Yan, and J. Yu, "Two-phase flow distribution in parallel flow mini/micro-channel heat exchangers for refrigeration and heat pump systems: A comprehensive review," Appl. Therm. Eng. **201**(PB), 117820 (2022).
[24]Z. Lei, X. Yang, C. Haberstroh, B. Pulko, S. Odenbach, and K. Eckert, "Space- and time-resolved interferometric measurements of the thermal boundary layer at a periodically magnetized gadolinium plate," Int. J. Refrig. **56**, 246–255 (2015).
[25]N. Kakuta, K. Kondo, H. Arimoto, and Y. Yamada, "Reconstruction of cross-sectional temperature distributions of water around a thin heating wire by inverse Abel transform of near-infrared absorption images," Int. J. Heat Mass Transfer **77**, 852–859 (2014).
[26]N. Kakuta, Y. Arakawa, M. Kyoda, T. Miyake, K. Mishiba, and K. Kondo, "Near-infrared measurement of axisymmetric temperature field formed by free convection from a 1-mm-diameter heating sphere in water," Int. J. Heat Mass Transfer **137**, 847–856 (2019).
[27]T. A. Nguyen, K. Kondo, and N. Kakuta, "Near-infrared measurement of temperature fields formed by mixed convection from a small heating sphere in water," Int. J. Therm. Sci. **176**, 107498 (2022).
[28]V. C. Han and N. Kakuta, "Near-infrared measurement of water temperature near micro-magnetic particle layer in a fluidic channel under induction heating," Exp. Therm. Fluid Sci. **115**, 110087 (2020).
[29]T. Uema, T. Ohata, Y. Washizuka, R. Nakanishi, D. Kawashima, and N. Kakuta, "Near-infrared imaging in a microfluidic channel of aqueous acid–base reactions," Chem. Eng. J. **403**, 126338 (2021).
[30]T. A. Nguyen and N. Kakuta, "Experimental study on the initial thermal plumes produced by small heating plates in water," Exp. Therm. Fluid Sci. **142**, 110803 (2023).
[31]Y. Ozaki, C. W. Huck, S. Tsuchikawa, and S. B. Engelsen, *Near-Infrared Spectroscopy* (Springer, Singapore, 2021).
[32]M. Iwasaka and S. Ueno, "Structure of water molecules under 14 T magnetic field," J. Appl. Phys. **83**(11), 6459–6461 (1998).
[33]K. X. Zhou, G. W. Lu, Q. C. Zhou, J. H. Song, S. T. Jiang, and H. R. Xia, "Monte Carlo simulation of liquid water in a magnetic field," J. Appl. Phys. **88**(4), 1802–1805 (2000).
[34]N. Kakuta, K. Nishijima, K. Kondo, and Y. Yamada, "Near-infrared measurement of water temperature near a 1-mm-diameter magnetic sphere and its heat generation rate under induction heating," J. Appl. Phys. **122**(4), 044901 (2017).
[35]R. Almeida, S. C. Freitas, C. R. Fernandes, R. Kiefe, J. P. Araújo, J. S. Amaral, J. O. Ventura, J. H. Belo, and D. J. Silva, "Rotating magnetocaloric effect in polycrystals—Harnessing the demagnetizing effect," J. Phys. Energy **6**(1), 015020 (2024).
[36]A. Aharoni, "Demagnetizing factors for rectangular ferromagnetic prisms," J. Appl. Phys. **83**(6), 3432–3434 (1998).
[37]Y. Hirayama, R. Iguchi, X. F. Miao, K. Hono, and K. Uchida, "High-throughput direct measurement of magnetocaloric effect based on lock-in thermography technique," Appl. Phys. Lett. **111**(16), 163901 (2017).
[38]K. K. Nielsen, C. R. H. Bahl, and A. Smith, "Constraints on the adiabatic temperature change in magnetocaloric materials," Phys. Rev. B **81**(5), 1–5 (2010).
[39]N. Otsu, "A threshold selection method from gray-level histograms," IEEE Trans. Syst. Man Cybern. **9**(1), 62–66 (1979).
[40]Y. Jiang, B. Nie, Y. Zhao, J. Carmeliet, and F. Xu, "Scaling of buoyancy-driven flows on a horizontal plate subject to a ramp heating of a finite time," Int. J. Heat Mass Transfer **171**, 121061 (2021).
[41]Y. Fan, Y. Zhao, J. F. Torres, F. Xu, C. Lei, Y. Li, and J. Carmeliet, "Natural convection over vertical and horizontal heated flat surfaces: A review of recent progress focusing on underpinnings and implications for heat transfer and environmental applications," Phys. Fluids **33**(10), 101301 (2021).
[42]K. K. Nielsen, C. R. H. Bahl, and K. Engelbrecht, "The effect of flow maldistribution in heterogeneous parallel-plate active magnetic regenerators," J. Phys. D: Appl. Phys. **46**(10), 105002 (2013).
[43]S. Li, H. Zhang, J. Cheng, X. Li, W. Cai, Z. Li, and F. Li, "A state-of-the-art overview on the developing trend of heat transfer enhancement by single-phase flow at micro scale," Int. J. Heat Mass Transfer **143**, 118476 (2019).